Materials Advances

ROYAL SOCIETY OF CHEMISTRY

PAPER

View Article Online
View Journal | View Issue

Cite this: *Mater. Adv.*, 2023, 4, 5594

Ultra-bright and thermally stable deep red emitting doped yttrium zirconate nanoparticles for tunable white LEDs and indoor plant growth

Reshmi Thekke Parayil,[ac] Santosh Kumar Gupta,[*ac] Malini Abraham,[bd] Subrata Das,[bd] Shreyas S. Pitale,[e] Kathi Sudarshan[ac] and Manoj Mohapatra[ac]

To counter the problem of the lack of an efficient red phosphor in commercial LEDs, it is important to develop a red-emitting phosphor with a high quantum efficiency, thermal stability, and size of nanodomain. The present work involves the synthesis of deep red-emitting $Y_2Zr_2O_7:Eu^{3+}$ (YZOE) nanocrystals with a very high color purity, excellent thermal stability, and a higher absolute photoluminescence quantum yield (PLQY) value. The photoluminescence (PL) lifetime and positron annihilation lifetime spectroscopy (PALS) suggested that a very large fraction of the Eu^{3+} ions occupy an isovalent Y^{3+} site with a minimal lattice strain. Triggered by this, the absolute PLQYs for the YZOE nanocrystals reach over 88%, which is much higher than that of its bulkier counterpart, and the highest among the known Eu^{3+}-doped oxide based red-emitting phosphors. The color purity of the material (97%) is higher than that of the commercial red phosphor $Y_2O_3:Eu^{3+}$ (92.4%). The optimum red phosphor is able to retain a color purity of 89% at 428 K relative to the PL intensity observed at room temperature, and the activation energy is estimated to be 0.2 eV which demonstrates its excellent thermal stability. Interestingly, the designed red phosphor-converted (pc-LED) was able to provide the reference spectral region which is required for indoor plant growth. Finally, the tunable white LEDs (cool and warm white LED) are fabricated by combining the RGB mixture of the optimized red YZOE nanoparticles with commercial green and blue phosphors together with a 280 nm UV LED chip. By tuning the RGB mixing ratio, the resultant emission from the fabricated pc-LED appears as a warm white light with a correlated color temperature (CCT) of 4164 K, color rendering index (CRI) of 78, and CIE of 0.358, 0.309 which is the ultimate requirement for ideal indoor lighting.

Received 21st July 2023,
Accepted 10th October 2023

DOI: 10.1039/d3ma00442b

rsc.li/materials-advances

1. Introduction

Lighting consumes around 15% of the world's total energy demand, which is the main cause of 5% of the world's total greenhouse gas emissions as well as energy scarcity.[1,2] The two main factors that are responsible for this are population growth and increased urbanization which is further expected to increase the lighting demand to 50% by 2030.[2–4] These adverse scenarios mainly arise from the use of incandescent and fluorescent lamps which suffer from low light efficiency, high power consumption, and high heat generation.[5,6] It is expected that the use of light-emitting diodes (LEDs) can reduce lighting power consumption by half because of their high light efficiency, low power consumption, high durability, long life, lower heat generation, and eco-friendliness.[7–10] The current existing commercial white LED consists of an InGaN chip with Ce^{3+} activated yttrium aluminum garnet ($Y_3Al_5O_{12}:Ce^{3+}$) which is the yellow phosphor material.[11] But because of the lack of a red phosphor, the emitted white light has a low color rendering index (CRI, $R_a < 80$) and a high correlated color temperature (CCT > 4500 K), making it a more bluish-white light which is not considered ideal for indoor lighting.[12–14] Due to these limitations their uses have not been harnessed in the areas such as medical imaging, general illumination, indoor lighting, and so on. The CRI is defined as the ability of a light source to reveal the color of objects when compared to sunlight, and the CCT is defined as the color appearance of white LED, both of these are very important photophysical parameters for evaluating the performance of LEDs. The other ways in which the white light can be generated are by combining red, green, and blue (RGB) phosphors which are excited by using UV LED or by mixing red

[a] *Radiochemistry Division, Bhabha Atomic Research Centre, Mumbai 400085, India. E-mail: santoshg@barc.gov.in, santufrnd@gmail.com*
[b] *Materials Science and Technology Division, CSIR-National Institute for Interdisciplinary Science and Technology, Thiruvananthapuram, Kerala 695019, India*
[c] *Homi Bhabha National Institute, Anushaktinagar, Mumbai 400094, India*
[d] *Academy of Scientific and Innovative Research (AcSIR), Ghaziabad 201002, India*
[e] *Technical Physics Division, Bhabha Atomic Research Centre, Mumbai 400085, India*

and green phosphors which are excited using a blue LED chip.[15] The combination of RGB phosphors with a UV LED chip gives a wide range of phosphors that can be excited by UV irradiation rather than by blue irradiation.[16–18]

The currently available phosphors are nitrides, sulfides, and oxysulfides which have many limitations such as thermal and chemical instability, and a complex synthesis process.[19] The existing commercial red phosphors are Eu^{2+} activated systems ($Sr_2Si_5N_8$:Eu^{2+} and $CaAlSiN_3$:Eu^{2+}) which possess low color purity and low luminous efficiency due to the broadband emission originating from the f → d transitions of Eu^{2+} leading to the serious issue of photon reabsorption.[20–22] Comparing Eu^{3+} with Eu^{2+}, the former has a sharp red emission band due to the f → f transition.[22] Even though both are the same rare earth element, their luminescence properties are different due to the different electronic structures they possess. The other sulfide-based phosphor which is currently being used is Y_2O_2S:Eu^{3+} but it also suffers from poor absorption and stability issues with near UV light.[23] The sulfide-based phosphors also have the limitation that they release poisonous sulfur gas which is harmful to the environment.[24,25] Compared to nitrides and sulfides, oxide-based phosphors have the advantage of a high luminescence efficiency, good thermal and chemical stability, high vacuum stability, easy synthesis methods, and eco-friendliness.[25,26] Hence, the choice of the host becomes a very important criterion for designing an efficient lanthanide ion-doped phosphor.[5,16,27] The forbidden transition of the activator is relaxed when it is surrounded by the host matrix and because of this the luminescence intensity is enhanced.[9] So it is inevitable to develop a new oxide-based red phosphors with a high quantum yield efficiency, good thermal stability, strong absorption in the UV region, and an economically feasible synthesis route to cope the existing scenario.[28] As an activator for the phosphor material, Eu^{3+} is a promising candidate for red emission due to its unique properties such as narrow red emission, a sensitive transition which depends on the chemical surrounding, and the long lifetime of the chemical species.[26,29] The red emission is in the region from 603 to 630 nm which corresponds to the $^5D_0 \rightarrow {}^7F_2$ transition.

In addition to the white LEDs (w-LEDs), the phosphor converted LEDs (pc-LEDs) have acquired great attention as an artificial lighting source in the fields of modern agriculture and indoor plant growth applications, especially in areas that lack land and light resources.[30] Promoting plant growth is significant because this purifies the air providing a soothing environment and enables cheap and highly nutritional food to be available in all the seasons.[31] Pigments such as chlorophyll and phytochrome having a maximum absorption in the red region (known as P_R), and in the far-red region (known as P_{FR}), play a vital role in photosynthesis, phototropism, and photomorphogenesis which are essential for the processes like seed germination, formation of seedlings, and flowering. The absorption spectra of phytochromes cover a broad range of wavelengths from about 550 nm to 750 nm and that of chlorophyll covers the deep red emission region with a peak at about 660 nm. The phosphors with emissions overlapping the absorption spectra of plant photoreceptors can efficiently be utilized in the fabrication of red LEDs for plant growth.[32,33]

In this work we have utilized a gel-combustion technique to synthesize nanostructured YZOE and exposed it to different annealing temperatures to see if there was any observable photophysical change. The defects in the materials as a result of doping were probed using PALS, as they are known to have a very dominant role in fluorescence. Furthermore, the photoluminescence quantum yield (PLQY) was determined using an integrating sphere to harness the potential of YZOE for pc-LEDs. Electroluminescence (EL) measurement was carried out on the sample possessing the highest PLQY. The YZOE was further utilized to make a red LED and this was coupled with commercial green and blue phosphors to fabricate the wLED. The CRI and CCT values were improved by changing the composition of YZOE in the fabricated wLED. The thermal stability was also determined by carrying out *in situ* photoluminescence (PL) measurements. With a complete collection of photophysical measurements and physical characterization results, coupled with applications in pc-LEDs, the importance of this particular material as a potential candidate for red-emitting phosphor for commercial white light was highlighted. Also, the emission spectrum of the phosphor under study overlapped with the phytochrome absorption spectrum. Hence, this material can efficiently be utilized for plant growth applications.

2. Experimental

2.1. Synthesis

The starting materials used for the synthesis were: zirconium nitrate [$Zr(NO_3)_2{\cdot}5H_2O$, 99.9%], yttrium nitrate [$Y(NO_3)_3{\cdot}6H_2O$, 99.99%], europium nitrate [$Eu(NO_3)_3{\cdot}5H_2O$], and glycine (AR). Initially, the $Zr(NO_3)_2{\cdot}5H_2O$ and the $Y(NO_3)_3{\cdot}6H_2O$ solutions were prepared, and then mixed with an appropriate amount of glycine (fuel) solution. A suitable quantity of $Eu(NO_3)_3{\cdot}5H_2O$ was added to have Eu doping of 5 mol% in the final product. Then the mixture was stirred for 2 h to obtain a transparent solution which was then introduced into a muffle furnace which was preheated at 500 °C. The solution was allowed to boil and this forms a voluminous foamy combustion residue. Next, the white powders obtained were ground and then annealed at 900 °C for 1 h. This sample was labeled as YZOE-900. The as prepared samples were further ground and annealed to 1000, 1100, 1200, or 1300 °C for 1 h, and they were labeled as YZOE-1000, YZOE-1100, YZOE-1200, and YZOE-1300, respectively.

2.2. Characterization

To check the phase purity of the synthesized samples, X-ray diffraction (XRD) was carried out on a benchtop X-ray diffractometer with a step size of 0.02° and 2θ ranging from 15–80° with CuKα as the monochromatic source. The accelerating voltage and tube current were 30 kV and 20 mA, respectively. The Raman measurements were carried out on an AIRIX Corporation (formerly Seki) STR300 Laser Raman spectrometer. The spectrometer is equipped with a fiber-coupled diode-pumped

solid-state laser (DPSS) with an excitation wavelength of 532 nm. The TEM measurements were obtained using a Jeol JEM-2100 electron microscope with an applied voltage of 200 kV. The particle size and *d* spacing were calculated using ImageJ software. The PL measurements were carried out on an Edinburgh Instruments FLS1000 spectrometer with xenon lamp as the excitation source and photomultiplier tube (PMT) as the detector. The lifetime decay measurements were made by using a microsecond flash lamp as the source. The absolute quantum yield value was obtained by integrating a sphere module into the spectrometer. The positron annihilation lifetimes were measured on powder samples using a positron annihilation lifetime spectrometer (PALS) constructed from two BaF_2 scintillation detectors. The time resolution of the spectrometer was 243 ps and 10 μCi of Na-22 encapsulated in 8 μm polyimide film was used as the positron source. The spectra were analyzed using the PALSfit program. The EL properties and temperature-dependent PL characteristics were measured using an Ocean Optics Maya2000 Pro high-sensitivity spectrophotometer.

3. Results and discussion

3.1. Physical characterization

Fig. 1(a) shows the X-ray diffraction patterns of the as-prepared (at 900 °C) and the annealed YZOE materials at four different temperatures (1000 °C, 1100 °C, 1200 °C, 1300 °C). From Fig. 1 it is clear that the XRD pattern matches with the standard pattern for $Y_2Zr_2O_7$ shown in JCPDS no. 98-010-6029 which suggests the phase purity of the materials. No other additional peaks from the precursors or impurity are seen in the XRD pattern. The main peaks were at 29.7°, 34.4°, 49.5°, 58.8°, 61.7°, and 72.6° which corresponds to the (222), (400), (440), (622), (444), and (800) crystal planes, respectively, with the defect fluorite structure and the space group $Fm\bar{3}m$. The crystal structure for the defect fluorite is shown in Fig. 1(c). The enlarged XRD spectrum, shown to the right side, in the angle range from 28° to 37° shows the high intensity peaks. It is clear from the figure that with the increase in the annealing temperature the full width at half maximum (FWHM) of the peak is reduced from 900 to 1300 °C. Such a thermally induced peak narrowing is attributed to the increase in the particle size with temperature, which was also confirmed from the TEM study. Fig. 1(b) shows the Rietveld analysis of all the synthesized materials, and the cell parameter values are shown in Table 1. It was clear that with the increase in the annealing temperature, the cell parameters and cell volume had increased slightly. Fig. 1(d) shows the Raman spectra of all the materials. The weak intensity peak at 483 cm^{-1} was due to the A_{1g} mode responsible for the Zr–O bending mode,[34] and the high intensity peak at 650 cm^{-1} corresponds to the F_{2g} mode.[35] The ideal pyrochlore structure is known to possess a unique sextet feature in the Raman spectra enabled by six different vibrational modes $4F_{2g} + E_g + A_{1g}$. However, the defect fluorite structure shows broad Raman bands because seven O^{2-} ions are distributed randomly over the eight anionic sites leading to a high level of structural disordering.[36]

Fig. 1(e), (g), and (i) represent the TEM images and Fig. 1(f), (h), and (j) represent the particle size distributions of YZOE-900, YZOE-1000, and YZOE-1200, respectively. It is clearly seen that most of the particles have a nanospherical shape, although many of them adhere to each other to form small aggregates. From the size distribution plot, it can be seen that there was an increase in the particle size from ~54 to 77 nm. Also, with the increase in the annealing temperature, the crystalline growth of the particles can be seen. Fig. 1(k) and (l) show the high-resolution TEM (HRTEM) images of YZOE-1000 and YZOE-1200, and the insets show the magnified images with the lattice fringes. From these images, the lattice crystallographic orientation of the YZOE particles can be seen clearly, which suggests the presence of nano-polycrystals. The lattice fringes with the interplanar spacing value of 0.232/0.237 are assigned to the crystal planes of 2θ = 29.89 which suggests the formation of high quality cubic YZOE nanocrystals.

3.2. Time resolved photoluminescence

Fig. 2(a) shows the excitation spectra of the as-prepared sample as well as the annealed samples, with an emission wavelength of 607 nm. The spectra consist mainly of seven peaks, the one at 260 nm is due to the combined host absorption band and the charge transfer from $O^{2-} \rightarrow Eu^{3+}$.[37] The other peaks are due to the intra 4f → 4f transitions, and they are at 321, 362, 383, 393, 418, and 465 nm that correspond to the $^7F_0 \rightarrow {}^5H_6$ $^7F_0 \rightarrow {}^5D_4$, $^7F_0 \rightarrow {}^5L_7$, $^7F_0 \rightarrow {}^5L_6$, $^7F_0 \rightarrow {}^5D_3$, and $^7F_0 \rightarrow {}^5D_2$ transitions, respectively.

Fig. 2(b) and (d) are the emission spectra of the YZOE nanocrystals with excitation wavelengths of 265 and 395 nm, respectively, in which the former is the charge transfer band excitation, whereas the latter is the direct excitation of the europium. Both represent the same spectral features of Eu^{3+} with a difference in their intensities. There are mainly five peaks which are due to the $^5D_0 \rightarrow {}^7F_J$ (J = 0–4) transitions that can be observed in both spectra. The peaks at 579 and 712 nm correspond to the $^5D_0 \rightarrow {}^7F_0$ and $^5D_0 \rightarrow {}^7F_4$ transitions, respectively, which are electric dipole transitions. The $^5D_0 \rightarrow {}^7F_1$ transition is allowed by a magnetic dipole transition with a peak at 593 nm. The peak at 655 nm is due to the $^5D_0 \rightarrow {}^7F_3$ transition which is neither allowed by an electric or by a magnetic dipole transition. The higher intense transition at 610–630 nm is due to the $^5D_0 \rightarrow {}^7F_2$ transition which is hypersensitive due to the forced electric dipole transition. Fig. 2(c) and (e) represent the intensity of the $^5D_0 \rightarrow {}^7F_2$ peak with the annealing temperature for both the 264 and 395 nm excitation. As can be seen from the emission spectra, the $^5D_0 \rightarrow {}^7F_2$ transition has a higher intensity compared to the $^5D_0 \rightarrow {}^7F_1$ transition, which suggests that the surrounding environment of Eu is highly asymmetric and lacks a center of inversion. This is enabled by the fact that the former originates from hypersensitive electric dipole transitions whereas the latter is enabled by pure magnetic dipole transitions.[38] In the defect pyrochlore $Y_2Zr_2O_7$, both Y^{3+} and Zr^{4+} had a coordination number of 7, and the corresponding ionic radii were 96 and 78 pm, and for Eu^{3+}

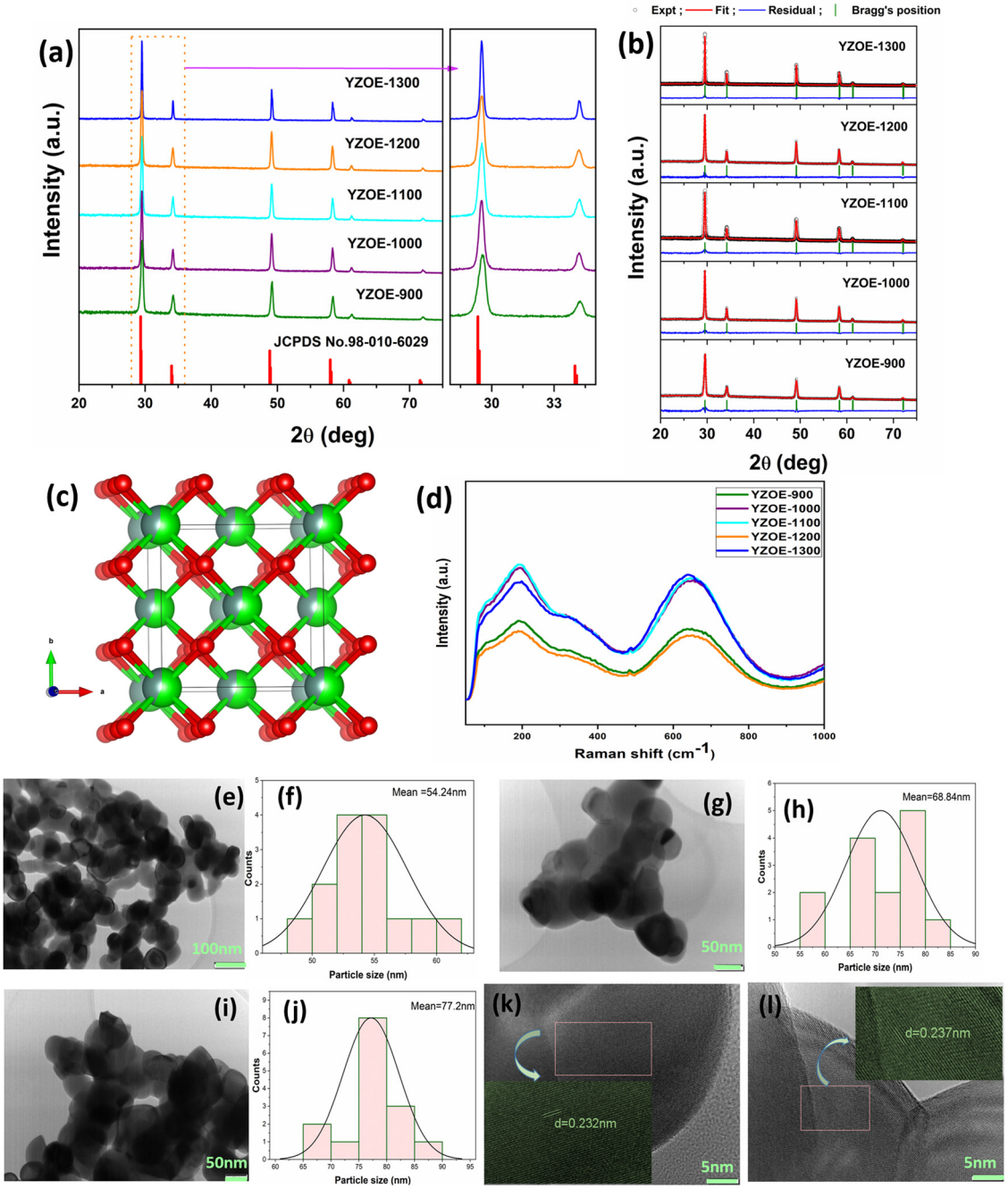

Fig. 1 (a) The XRD patterns, (b) the Rietveld refinement plot, (c) the crystal structure, and (d) the Raman spectra of YZOE annealed at different temperatures from 1100–1300 °C. (e), (g), and (i) The TEM images, (f), (h), and (j) the particle sizes of YZOE-900, YZOE-1000, and YZOE-1200, and (k) and (l) the HRTEM images of YZOE-1000 and YZOE-1200.

Table 1 The lattice parameters of $Y_2Zr_2O_7$:Eu

Annealing temperature (°C)	Lattice parameters $a = b = c$ (Å)	Unit cell volume (Å^3)
900	5.2414 (8)	144.00 (4)
1000	5.2431 (5)	144.14 (1)
1100	5. 2427 (7)	144.10 (3)
1200	5.2444 (6)	144.24 (4)
1300	5.2399 (2)	143.87 (1)

with a coordination number of 7, the ionic radius was 101 pm. Because of the close size as well as the charge matching, the Eu^{3+} tends to occupy the Y^{3+} site. However, we cannot rule out some fraction of the Eu^{3+} occupying the Zr^{4+} site with the additional creation of oxygen vacancies and antisite defects to compensate for the charge imbalance.

It can be seen from both Fig. 2(c) and (e) that the emission intensity increases monotonically with an increase in the annealing temperature with a slight dip at 1200 °C. The increase of PL

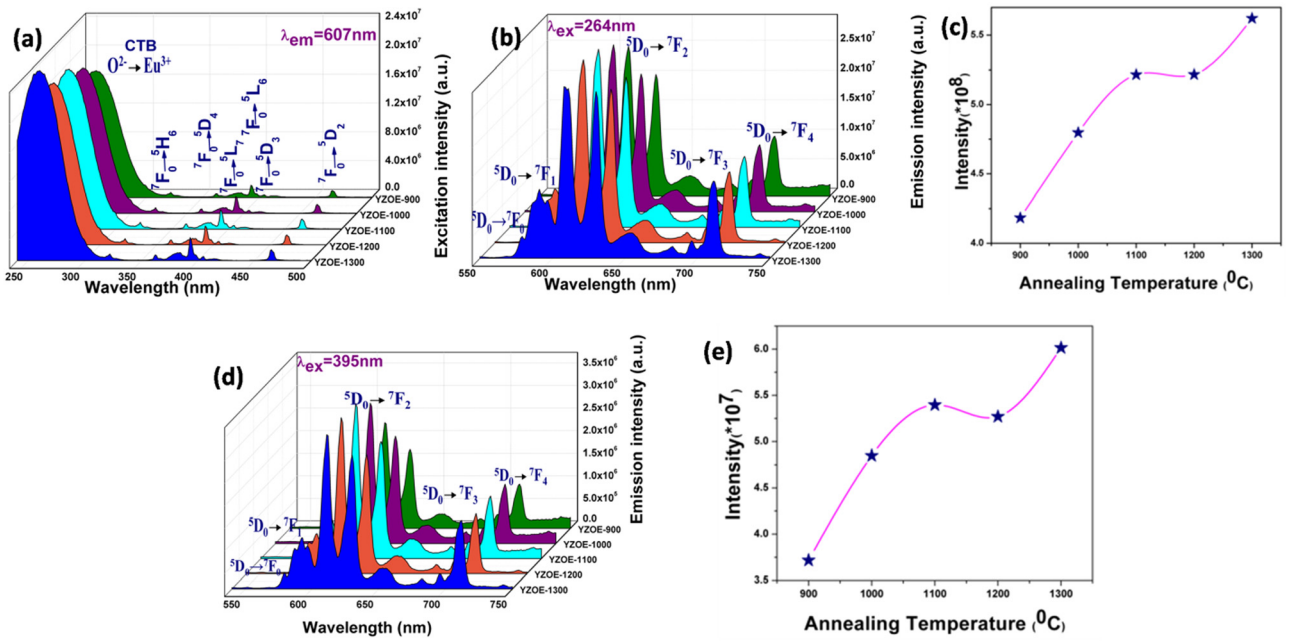

Fig. 2 (a) Excitation spectra under 607 nm emission, (b) emission spectra with 264 nm excitation, (c) variation in the integral intensity of the $^5D_0 \rightarrow {}^7F_2$ peak at 264 nm excitation, (d) the emission spectra with 395 nm excitation, and (e) the variation in integral intensity of the $^5D_0 \rightarrow {}^7F_2$ peak at 395 nm excitation of YZOE, with an annealing temperature from 900–1300 °C.

emission with the increase in annealing temperature was ascribed to the reduction in surface states which are known to provide non-radiative channels and lead to the reductions in PL and PLQY.[39]

Fig. 3(a) shows the decay curve of all the samples with an excitation wavelength of 264 nm and an emission wavelength of 607 nm, and Fig. 3(b) shows the decay curve with an excitation wavelength of 395 nm and an emission wavelength of 607 nm. Both the decay curves can be fitted into the bi-exponential equation which is given by:

$$I(t) = A_0 + A_1 \exp\left(\frac{-t}{\tau_1}\right) + A_2 \exp\left(\frac{-t}{\tau_2}\right) \quad (1)$$

where τ_1 and τ_2 are the decay values, and A_0, A_1, and A_2 are the scalar quantities obtained from the fitting. The fitted values are shown in Table 2. The two flourescence decay lifetime values suggest that Eu^{3+} is in two different chemical environments in the crystal lattice.However, the fraction of Eu^{3+} showing larger flourescence lifetime or slowly decaying species is higher (80–90%) than the Eu^{3+} showing shorter florescence lifetime (10–20%). Normally the short lifetime is due to Eu in an asymmetric environment whereas the long lifetime is due to Eu in more symmetrical site. From the emission data, it was found that the Eu^{3+} is occupying two sites which also supports the lifetime data. The longer lifetime with a very large population (~80–90%) is associated with the Eu^{3+} ion occupying the Y^{3+} site. This is a more conducive environment with no lattice strain or creation of any charge compensating defects enabled by close size and charge matching. The shorter lifetime with a smaller population is associated with some fraction of the Eu^{3+} ion which may be occupying the surface of the nanoparticles. This may provide some additional non-radiative channels and may reduce the emission output and the PLQY.

Fig. 3(c) is the plot of the absolute quantum yield against temperature, which was evaluated by using a barium sulfate coated integrating sphere as the reflectance standard background. With the increase in the annealing temperature, it was observed that there was an enhancement in the quantum yield up to 88.2% at 1200 °C, and a further increase in the annealing temperature reduced the quantum yield to 82.5%. The value of the internal quantum efficiency was calculated using eqn (2):[40,41]

$$\eta = \frac{\int L_s}{\int E_R - \int E_S} \quad (2)$$

where η is the internal quantum efficiency, L_S is the emission spectra of the sample, and E_R and E_S are the excitation spectra without a sample and with a sample, respectively.

Normally nanocrystalline samples have a lower PLQY value because of poor crystallinity and a high density of surface defects compared to their bulk counterparts. In this work we demonstrated that the YZOE nanocrystalline sample showed very high absolute PLQY of ~88%. This could have arisen from a very high concentration of Eu^{3+} ion occupying the Y^{3+} site which invoked no charge compensating defects, and minimal lattice strain because of the close size and charge matching. The corresponding spectrograms for all the samples are plotted in Fig. 3(d)–(h).

3.3. Defect evolution as a function of annealing temperature

The positron lifetime spectra (Fig. 4(a)) were analyzed with appropriate corrections for positron annihilations in the

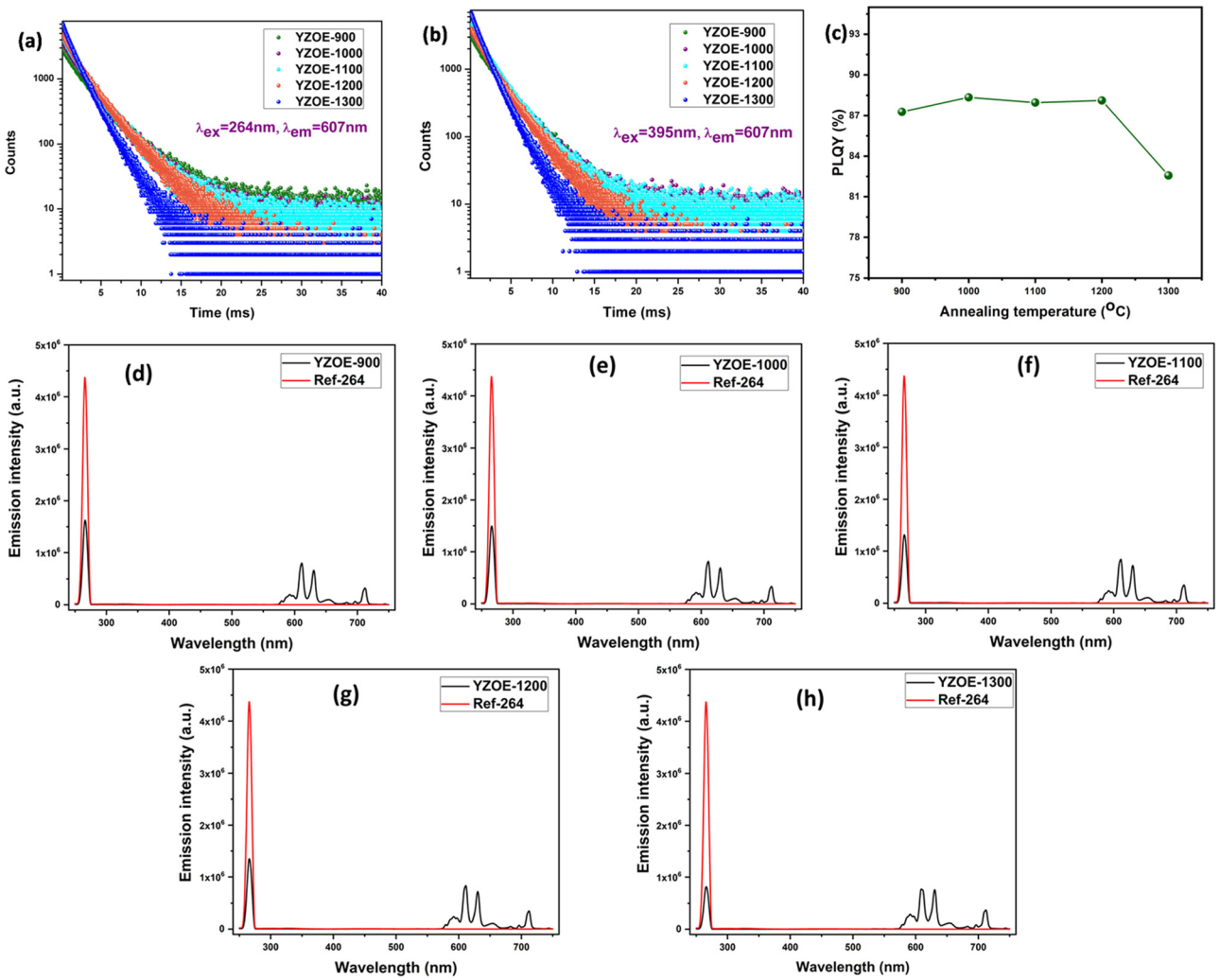

Fig. 3 (a) Lifetime decay curve with 264 nm excitation, (b) lifetime decay curve with 395 nm excitation, (c) absolute quantum yield values, and (d)–(h) spectrograms of YZOE with annealing temperatures from 900–1300 °C.

Table 2 Summary of the lifetime values of YZOE-900 to YZOE-1300

	λ_{ex} = 264 nm, λ_{em} = 607 nm				λ_{ex} = 395 nm, λ_{em} = 607 nm			
Sample	τ_1 (ms)	τ_2 (ms)	Population of τ_1 (%)	Population of τ_2 (%)	τ_1 (ms)	τ_2 (ms)	Population of τ_1 (%)	Population of τ_2 (%)
YZOE-900	1.7	3.7	15.2	84.8	1.6	3.3	15.2	85.8
YZOE-1000	1.6	3.5	12.1	87.9	1.6	3.3	16.4	83.6
YZOE-1100	1.6	3.4	14.2	85.8	1.5	3.2	18.6	81.4
YZOE-1200	1.5	3.3	10.6	89.4	1.4	2.9	10.9	89.1
YZOE-1300	1.1	2.2	19.5	80.5	1.1	2.1	19.4	80.6

polyimide film which encapsulated the Na-22. The spectra were fitted well to the sum of three exponentials or three lifetimes. The longest lifetime component in all of the samples was about 1.6–2.0 ns with only <1% contribution. However, the inclusion of this lifetime component was necessary to improve the quality of the fitting of the spectra. A lifetime component in this range with poor intensities is well known in powder samples and is attributed to the positronium formation on the surface of the particles and the intergranular spaces.

The other two positron lifetimes (τ_1 and τ_2), intensity of the second positron lifetime component (I_2, $I_1 \sim 100 - I_2$) and the average positron lifetime (τ_{av}) calculated as the intensity weighted average of the two positron lifetimes in the samples annealed at different temperatures, are shown in Fig. 4(b). Positron annihilation lifetimes are reported on similar compounds in the literature. Gregg *et al.*[42] reported a single positron lifetime of 211 ps in $Gd_2Zr_2O_7$ whereas Gumber *et al.*[43] reported an average lifetime of 218.5 ps. Two lifetime components were

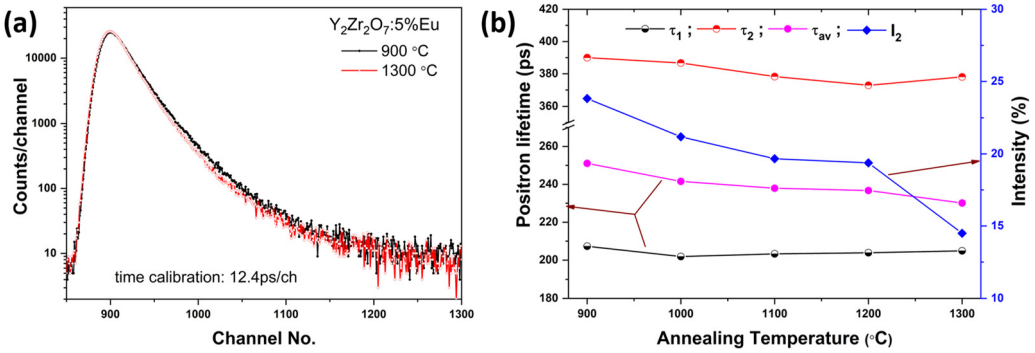

Fig. 4 (a) Typical positron annihilation lifetime spectra of $Y_2Zr_2O_7$:5% Eu annealed at 900 °C and 1300 °C, and (b) positron annihilation lifetimes and intensities in $Y_2Zr_2O_7$:5% Eu annealed at different temperatures.

observed earlier in $Nd_2Zr_2O_7$ annealed at different temperatures[39] and in Sm doped $Gd_2Zr_2O_7$.[44] In all these systems where two positron lifetime components were observed, the first component was due to the positron annihilations in the bulk whereas the second component was due to the positron annihilations in the defects. It can be seen from Fig. 4(b); the variation in τ_1 with an increase in annealing temperature is marginal. A small but monotonous decrease was observed in the second positron lifetime component. The intensity of the second positron lifetime or the fraction of positrons trapped in the defects which reflected the defect concentration decreased with the increase in annealing temperature. This decrease was significant in the sample annealed at 1300 °C. The average positron lifetime also showed a gradual decrease with the increase in annealing temperature. The change in the average lifetime with annealing temperature was similar to earlier observations on $Nd_2Zr_2O_7$.[39]

3.4. Temperature-dependent photoluminescence studies

Fig. 5(a) shows the variation of PL intensity for the representative sample, YZOE-1200, under 280 nm excitation for a range of temperatures starting from room temperature to 448 K. Even though the emission intensity was exhibiting a decreasing trend with the rise in temperature, its value at 428 K was estimated to be about 88.9% of that of the room temperature intensity. This implied that the phosphor had adequate thermal stability making it useful for lighting applications. As seen in the inset of Fig. 5(a), the activation energy for thermal quenching could be evaluated from the relationship between the relative emission intensities and the corresponding temperature using eqn (3):

$$I(T) = \frac{I_0}{1 + \alpha \cdot \exp\left(-\frac{E_a}{KT}\right)} \quad (3)$$

where I_0 is the room temperature emission intensity, $I(T)$ is the emission intensity at different temperatures, α is the rate constant, E_a is the activation energy for thermal quenching, and K is the Boltzmann constant.[45] From the plot of $\ln((I_0/I(T)) - 1)$ *versus* $1/KT$, the experimental data could be linearly fitted with a slope of 0.2, which was therefore the activation energy for the sample. The variation of peak intensity with temperature at 611 nm is shown in Fig. 5(b). The emission spectra show a gradual decrease in intensity with the increase in temperature. The CIE coordinates variation with temperature in Fig. 5(b) shows that there was not much variation in the CIE coordinate values with the increase in temperature.

The thermal stability, activation energy, and color purity of various recently reported Eu^{3+} doped phosphors, together with their excitation and emission peaks, are listed in Table 3. It was

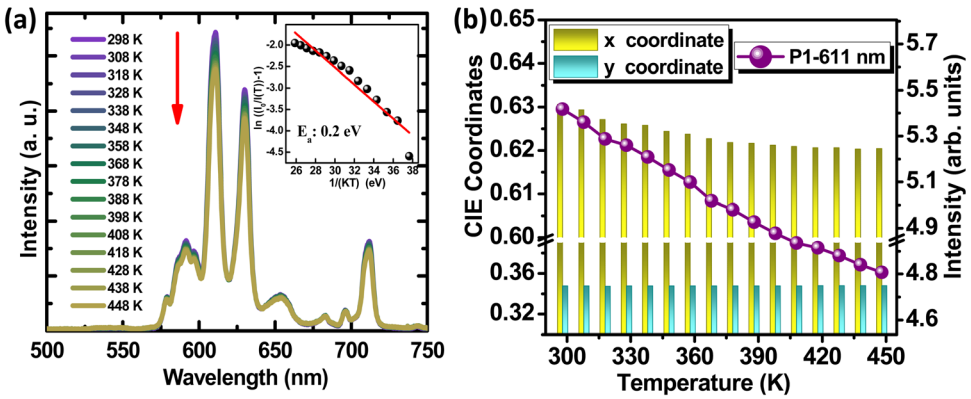

Fig. 5 (a) The temperature dependent PL spectra for the YZOE-1200 phosphor under excitation of 280 nm for a range of temperatures from 298 K to 448 K. The inset shows the fitting of the PL intensities using the Arrhenius equation with the corresponding activation energy. (b) A bar diagram showing the CIE coordinates and the peak intensity variation with temperature at 611 nm for the YZOE-1200 phosphor.

Table 3 The recently reported Eu^{3+} doped phosphors with the corresponding thermal stability values, activation energy, and color purity

Sample	λ_{ex} (nm)	λ_{em} (nm)	I (423 K)/I_0 (%)	E_a (eV)	Color purity (%)	Ref.
$ZnAl_2O_4:Eu^{3+}$	394	614	87.59	0.11	90.39	46
$ZnAl_2O_4:Eu^{3+}$, Li^+	394	614	96.03	0.14	92.02	46
$Y_2SiWO_8:Eu^{3+}$	395	619	81.7	0.12	96.6	47
$Ca_3Al_2Ge_3O_{12}:Eu^{3+}$	394	707	78.8	0.16	—	48
$CaMgGeO_4:Eu^{3+}$, Li^+	464	612	77	0.19	94	49
$Sr_2InTaO_6:Eu^{3+}$	396	624	66.4	0.20	96.4	8
YZOE-1200	280	611	88.9	0.20	97	This work

observed that the YZOE-1200 phosphor had a comparatively higher activation energy, exhibiting a high thermal stability ($I(T)/I_0$ = 88.9% at 423 K). Hence, this nanophosphor with high color purity can efficiently be utilized for phosphor-converted white LED applications.

3.5. LED fabrication

3.5.1. Fabrication of the red LED, demonstrating its feasibility for indoor plant growth. In order to evaluate the potential of the YZOE-1200 red phosphor in pc-LEDs, a red LED was fabricated by combining the optimized red phosphor with a 280 nm UV-LED chip. The corresponding EL spectra with the direct red LED images are shown in Fig. 6(a). The relevant CIE diagram is shown in Fig. 6(b) together with the direct image of the red pc-LED. It is evident from Fig. 6(b) that the estimated CIE coordinates (0.63, 0.35) for the emission from the pc-LED made with the optimized YZO:Eu^{3+} was situated in the deep red region. This is very close to the value of red emission (0.667, 0.326) reported for the commercial $Y_2O_2S:Eu^{3+}$ red phosphor,[50] and the red CIE coordinates (0.67, 0.33) standardized by the National Television Standard Committee was (0.67, 0.33).[51] Meanwhile, the color purity of the pc-LED exhibiting red emission was also calculated using a formula reported elsewhere,[50] which was estimated to be 97%. Therefore, the present research reported an optimized red phosphor with adequate quantum efficiency, high thermal stability, and high red color purity. An efficient red phosphor with such characteristics is very useful not only in display applications but also can be effectively utilized in making w-LEDs with improved color rendering (R_a) and CCT.

An efficient plant growth application using the red YZOE-1200 pyrochlore phosphors has also been identified. As shown in Fig. 6(a), the EL spectrum of Eu^{3+} is actually situated in the overall P_R and P_{FR} regions. Particularly, the $^5D_0$–$^7F_4$ peak located at 700 nm overlapped with the intense P_{FR} peak, which was crucial in stimulating seed propagation and plant growth.[51–53] Hence, as a smart approach, the deep red emission of the developed optimized red emitting phosphor can be utilized to fabricate deep red pc-LEDs for use as a promising artificial light source for cultivating indoor plants.[52,53]

3.5.2. Fabrication of a prototype white LED. For evaluating the real-time device performance of the optimized sample, a prototype white-LED was fabricated by combining a 280 nm UV chip with an operational voltage of 12 V and a current of 2 A, and a mixture of tri-color emitting phosphors by mixing optimum 1200 °C annealed YZO:Eu^{3+} red phosphor (YZOE-1200), and commercial blue (BAM:Eu^{2+}) and green (CMA:Tb^{3+}) phosphors with various mixing ratios. The resultant EL spectra for the various mixing combinations are given in Fig. 7(a). The corresponding chromaticity diagram is shown in Fig. 7(b), and the estimated color coordinates are listed in Fig. 7(c). As seen from Fig. 7, the white-LED obtained with a RGB mixing ratio of 4 : 2 : 2 showed a bright but cool white light, with a luminous efficacy of radiation (LER) of 239 lm W^{-1}, a CCT of 6624 K, a CRI (R_a) of 70, and CIE chromaticity coordinates of (0.320, 0.268). Such a bright cool white light was visible from the digital image of the fabricated pc-LED, as shown in inset (I) of Fig. 7(a). By tuning the RGB mixing ratio to 5 : 3 : 2, warm white light with the LER of 233 lm W^{-1}, CCT of 4164 K, R_a of 78, and CIE of (0.358, 0.309) has been produced from the fabricated pc LED, as appeared in the inset (III) of Fig. 7(a). These characteristic features are the ultimate requirements for indoor lighting for strain free viewing.

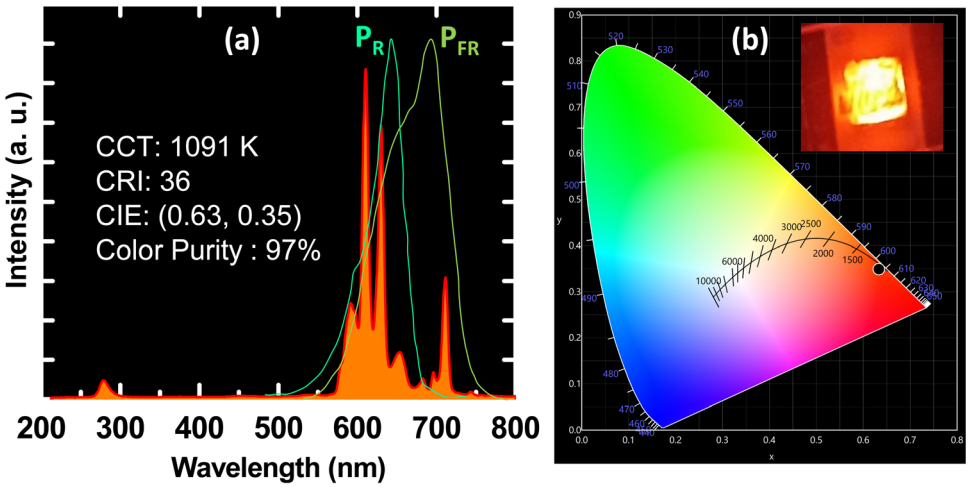

Fig. 6 (a) The electroluminescence spectra for the YZOE samples under 280 nm LED, and (b) the CIE color diagram with the corresponding LED image under 280 nm excitation.

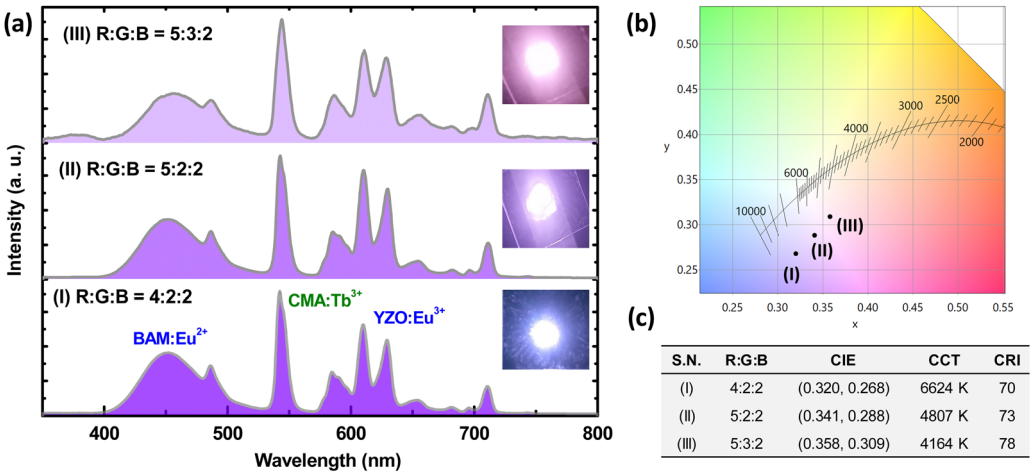

S.N.	R:G:B	CIE	CCT	CRI
(I)	4:2:2	(0.320, 0.268)	6624 K	70
(II)	5:2:2	(0.341, 0.288)	4807 K	73
(III)	5:3:2	(0.358, 0.309)	4164 K	78

Fig. 7 (a) The EL spectra for the wLED fabricated by combining the YZOE-1200 red phosphor with commercial green and blue phosphors in different ratios using a 280 nm UV-LED chip. (b) The corresponding CIE color diagram, and (c) the tabulated values of CIE, CCT, and CRI.

4. Conclusion

In this work we have synthesized bright and thermally stable, deep red emitting YZOE nanoparticles using gel combustion. The synthesized nanoparticles were subjected to a complete quality check using XRD, Raman spectroscopy, TEM, and PALS. A PLQY of more than 80% was achieved in all the samples, and samples annealed at 1200 °C showed a maximum PLQY of ~89%. The same particles were utilized in designing a pc-LED which showed a deep red emission with a CIE index value matching closely with that of a commercial red phosphor, and with improved color purity and excellent thermal stability. The deep red emission of the YZOE-1200 nanoparticles significantly overlapped with the absorption of phytochrome (P_{FR}), suggesting that this material showed a good potential for moderating plant growth. For evaluating the real-time device performance of the YZOE nanoparticles, a prototype wLED was fabricated by combining a 280 nm UV chip and a mixture of tri-color emitting phosphors. In fact, by tuning the RGB phosphor composition, both cool and warm w-LEDs were achieved. By tuning the RGB mixing ratio to 5 : 3 : 2, the resultant emission from the fabricated pc-LED appeared as a warm white light with a CCT of 4164 K, a R_a of 78, and a CIE of (0.358, 0.309), which was close to natural lighting.

Conflicts of interest

There are no conflicts to declare.

Acknowledgements

The authors would like to acknowledge Dr Sai Santosh Kumar Raavi, IIT Hyderabad for his help with the TEM measurements.

References

1 S. K. Gupta, K. Sudarshan, B. Modak and R. Gupta, Interstitial Zinc Boosted Light Tunability, Afterglow, and Ultrabright White Emission in Zinc Germanate (Zn_2GeO_4), *ACS Appl. Electron. Mater.*, 2023, **5**(2), 1286–1294.
2 H. Zhang, H. Zhang, A. Pan, B. Yang, L. He and Y. Wu, Rare earth-free luminescent materials for WLEDs: recent progress and perspectives, *Adv. Mater. Technol.*, 2021, **6**(1), 2000648.
3 Y. Liu, D. Yao and H. Zhang, Self-assembly driven aggregation-induced emission of copper nanoclusters: a novel technology for lighting, *ACS Appl. Mater. Interfaces*, 2017, **10**(15), 12071–12080.
4 A. Menéndez-Velázquez, D. Morales and A. B. García-Delgado, Sunlike white light-emitting diodes based on rare-earth-free luminescent materials, *Materials*, 2022, **15**(5), 1680.
5 S. K. Gupta, K. Sudarshan and R. Kadam, Optical nano-materials with focus on rare earth doped oxide: A Review, *Mater. Today Commun.*, 2021, **27**, 102277.
6 J. McKittrick and L. E. Shea-Rohwer, Down conversion materials for solid-state lighting, *J. Am. Ceram. Soc.*, 2014, **97**(5), 1327–1352.
7 Y. Zhang, J. Xu, Q. Cui and B. Yang, Eu^{3+}-doped $Bi_4Si_3O_{12}$ red phosphor for solid state lighting: microwave synthesis, characterization, photoluminescence properties and thermal quenching mechanisms, *Sci. Rep.*, 2017, **7**(1), 42464.
8 J. Zhao, H. Gao, H. Xu, Z. Zhao, H. Bu, X. Cao, L. He, Z. Yang and J. Sun, Structure and photoluminescence of Eu^{3+} doped Sr_2InTaO_6 red phosphor with high color purity, *RSC Adv.*, 2021, **11**(14), 8282–8289.
9 S. K. Gupta, R. M. Kadam and P. K. Pujari, Lanthanide spectroscopy in probing structure-property correlation in multi-site photoluminescent phosphors, *Coord. Chem. Rev.*, 2020, **420**, 213405.
10 J. Tian and W. Zhuang, Thermal stability of nitride phosphors for light-emitting diodes, *Inorg. Chem. Front.*, 2021, **8**(22), 4933–4954.
11 T. Hasegawa, M. Iwaki, R. Tanaka, S.-W. Kim, S. Yin and K. Toda, Phase stabilization of red-emitting olivine-type NaMgPO4:Eu^{2+} phosphors *via* molten-phase quenching, *Inorg. Chem. Front.*, 2020, **7**(21), 4040–4051.

12 X. Huang, Red phosphor converts white LEDs, *Nat. Photonics*, 2014, **8**(10), 748–749.
13 J. Meyer and F. Tappe, Photoluminescent materials for solid-state lighting: state of the art and future challenges, *Adv. Opt. Mater.*, 2015, **3**(4), 424–430.
14 S. K. Gupta, J. P. Zuniga, M. Abdou, P. S. Ghosh and Y. Mao, Optical properties of undoped, Eu^{3+} doped and Li^{+} co-doped $Y_2Hf_2O_7$ nanoparticles and polymer nanocomposite films, *Inorg. Chem. Front.*, 2020, **7**(2), 505–518.
15 J. Xie, L. Cheng, H. Tang, Z. Wang, H. Sun, L. Lu, X. Mi, Q. Liu and X. Zhang, Wide range color tunability and efficient energy transfer of novel $NaCaGd(WO_4)_3$:Tb^{3+},Eu^{3+} phosphors with excellent thermal stability for pc-WLEDs, *Inorg. Chem. Front.*, 2021, **8**(20), 4517–4527.
16 S. K. Gupta, J. P. Zuniga, M. Abdou, M. P. Thomas, M. De Alwis Goonatilleke, B. S. Guiton and Y. Mao, Lanthanide-doped lanthanum hafnate nanoparticles as multicolor phosphors for warm white lighting and scintillators, *Chem. Eng. J.*, 2020, **379**, 122314.
17 M. Qu, H. Li, Y. Zhao and X.-M. Zhang, Single-Component Color-Tunable $Gd(pic)_3$:Eu^{3+} Phosphor Based on a Metal–Organic Framework for Near-UV White-Light-Emitting Diodes, *ACS Omega*, 2019, **4**(2), 3593–3600.
18 D. F. Sava, L. E. Rohwer, M. A. Rodriguez and T. M. Nenoff, Intrinsic broad-band white-light emission by a tuned, corrugated metal–organic framework, *J. Am. Chem. Soc.*, 2012, **134**(9), 3983–3986.
19 M. Jiao, N. Guo, W. Lü, Y. Jia, W. Lv, Q. Zhao, B. Shao and H. You, Synthesis, structure and photoluminescence properties of europium-, terbium-, and thulium-doped $Ca_3Bi(PO_4)_3$ phosphors, *Dalton Trans.*, 2013, **42**(34), 12395–12402.
20 W. Geng, X. Zhou, A. Deng, W. Li and L. Zhao, Multiple charge transfer bands induced broad excitation Eu^{3+} red emission in a vanadium phosphate system for white light-emitting diodes, *Inorg. Chem.*, 2022, **61**(21), 8291–8297.
21 Y. Zhuo, S. Hariyani, E. Armijo, Z. Abolade Lawson and J. Brgoch, Evaluating thermal quenching temperature in Eu^{3+}-substituted oxide phosphors *via* machine learning, *ACS Appl. Mater. Interfaces*, 2019, **12**(5), 5244–5250.
22 A. Balhara, S. K. Gupta, G. D. Patra, B. Modak, J. Prakash, K. Sudarshan and M. Mohapatra, Stabilization of Eu^{2+} in $Li_2B_4O_7$ with the BO_3 network through U^{6+} co-doping and defect engineering, *Phys. Chem. Chem. Phys.*, 2023, **25**(3), 1889–1902.
23 H. Li, H. M. Noh, B. K. Moon, B. C. Choi, J. H. Jeong, K. Jang, H. S. Lee and S. S. Yi, Wide-band excited $Y_6(WMo)_{0.5}O_{12}$:Eu red phosphor for white light emitting diode: structure evolution, photoluminescence properties, and energy transfer mechanisms involved, *Inorg. Chem.*, 2013, **52**(19), 11210–11217.
24 S. K. Gupta, M. Mohapatra, S. Kaity, V. Natarajan and S. V. Godbole, Structure and site selective luminescence of sol–gel derived Eu:Sr_2SiO_4, *J. Lumin.*, 2012, **132**(6), 1329–1338.
25 K. Singh, M. Rajendran, R. Devi and S. Vaidyanathan, Narrow-band red-emitting phosphors with high color purity, trifling thermal and concentration quenching for hybrid white LEDs and $Li_3Y_3BaSr(MoO_4)_8$:Sm^{3+}, Eu^{3+}-based deep-red LEDs for plant growth applications, *Inorg. Chem.*, 2022, **61**(6), 2768–2782.
26 M. Rajendran and S. Vaidyanathan, Systematic investigation of Eu^{3+} activated $Na_2Ln_4(MoO_4)_7$ [Ln = La, Gd and Y] narrow band red emitting phosphors for hybrid white LEDs and plant growth, *New J. Chem.*, 2020, **44**(35), 14823–14836.
27 M. Pokhrel, S. K. Gupta, A. Perez, B. Modak, P. Modak, L. A. Lewis and Y. Mao, Up- and Down-Convertible LaF_3: Yb,Er Nanocrystals with a Broad Emission Window from 350 nm to 2.8 μm: Implications for Lighting Applications, *ACS Appl. Nano Mater.*, 2021, **4**(12), 13562–13572.
28 S. K. Gupta, B. Modak, P. Modak and Y. Mao, White light emission from co-doped La2Hf2O7 nanoparticles with suppressed host → Eu^{3+} energy transfer *via* a U^{6+} co-dopant, *Inorg. Chem. Front.*, 2021, **8**, 3830–3842.
29 T. Sreena, P. P. Rao, A. K. Raj and T. A. Thara, Exploitation of Eu^{3+} red luminescence through order–disorder structural transitions in lanthanide stannate pyrochlores for warm white LED applications, *Phys. Chem. Chem. Phys.*, 2018, **20**(37), 24287–24299.
30 Q. Sun, S. Wang, B. Devakumar, L. Sun, J. Liang and X. Huang, Synthesis, crystal structure, and photoluminescence characteristics of high-efficiency deep-red emitting Ba_2GdTaO_6:Mn^{4+} phosphors, *ACS Omega*, 2019, **4**(8), 13474–13480.
31 L. Sun, B. Devakumar, J. Liang, S. Wang, Q. Sun and X. Huang, Novel high-efficiency violet-red dual-emitting Lu_2GeO_5:Bi^{3+},Eu^{3+} phosphors for indoor plant growth lighting, *J. Lumin.*, 2019, **214**, 116544.
32 J. Long, X. Yuan, C. Ma, M. Du, X. Ma, Z. Wen, R. Ma, Y. Wang and Y. Cao, Strongly enhanced luminescence of Sr4Al14O25:Mn^{4+} phosphor by co-doping B^{3+} and Na^{+} ions with red emission for plant growth LEDs., *RSC Adv.*, 2018, **8**(3), 1469–1476.
33 M. Rajendran and S. Vaidyanathan, Zero-concentration quenching: a novel Eu^{3+} based red phosphor with non-layered crystal structure for white LEDs and NaSrY(MoO4)$_3$:Sm^{3+} based deep-red LEDs for plant growth, *Dalton Trans.*, 2020, **49**(27), 9239–9253.
34 M. de los Reyes, K. R. Whittle, Z. Zhang, S. E. Ashbrook, M. R. Mitchell, L.-Y. Jang and G. R. Lumpkin, The pyrochlore to defect fluorite phase transition in $Y_2Sn_{2-x}Zr_xO_7$, *RSC Adv.*, 2013, **3**(15), 5090–5099.
35 S. K. Gupta, M. A. P. Garcia, J. P. Zuniga, M. Abdou and Y. Mao, Visible and ultraviolet upconversion and near infrared downconversion luminescence from lanthanide doped $La_2Zr_2O_7$ nanoparticles, *J. Lumin.*, 2019, **214**, 116591.
36 S. K. Gupta, M. Abdou, P. S. Ghosh, J. P. Zuniga and Y. Mao, Thermally induced disorder–order phase transition of $Gd_2Hf_2O_7$:Eu^{3+} nanoparticles and its implication on photo-and radioluminescence, *ACS Omega*, 2019, **4**(2), 2779–2791.
37 M. Keskar, S. K. Gupta, R. Phatak, S. Kannan and V. Natarajan, Optical properties of Eu^{3+} activated thorium molybdate and thorium tungstate: Structure, local symmetry

and photophysical properties, *J. Photochem. Photobiol., A*, 2015, **311**, 59–67.

38 R. Mani, H. Jiang, S. K. Gupta, Z. Li and X. Duan, Role of Synthesis Method on Luminescence Properties of Europium(II, III) Ions in β-Ca_2SiO_4: Probing Local Site and Structure, *Inorg. Chem.*, 2018, **57**(3), 935–950.

39 S. K. Gupta, K. Sudarshan, P. Ghosh, A. Srivastava, S. Bevara, P. Pujari and R. Kadam, Role of various defects in the photoluminescence characteristics of nanocrystalline $Nd_2Zr_2O_7$: an investigation through spectroscopic and DFT calculations, *J. Mater. Chem. C*, 2016, **4**(22), 4988–5000.

40 K. Li, H. Lian, M. Shang and J. Lin, A novel greenish yellow-orange red $Ba_3Y_4O_9$:Bi^{3+},Eu^{3}+ phosphor with efficient energy transfer for UV-LEDs, *Dalton Trans.*, 2015, **44**(47), 20542–20550.

41 J. Zhong, D. Chen, Y. Zhou, Z. Wan, M. Ding, W. Bai and Z. Ji, New Eu^{3+}-activated perovskite $La_{0.5}Na_{0.5}TiO_3$ phosphors in glass for warm white light emitting diodes, *Dalton Trans.*, 2016, **45**(11), 4762–4770.

42 D. J. Gregg, Z. Zhang, G. J. Thorogood, B. J. Kennedy, J. A. Kimpton, G. J. Griffiths, P. R. Guagliardo, G. R. Lumpkin and E. R. Vance, Cation antisite disorder in uranium-doped gadolinium zirconate pyrochlores, *J. Nucl. Mater.*, 2014, **452**(1–3), 474–478.

43 N. Gumber, R. V. Pai, R. Phatak, B. Adiraju, M. Sahu, J. Jagannath and K. Sudarshan, Synthesis, characterization and crystal chemistry of uranium and cerium doped yttrium titanate pyrochlore: A potential waste immobilization matrix, *J. Nucl. Mater.*, 2021, **556**, 153191.

44 S. K. Gupta, C. Reghukumar, K. Sudarshan, P. Ghosh, N. Pathak and R. Kadam, Orange-red emitting $Gd_2Zr_2O_7$:Sm^{3+}: Structure-property correlation, optical properties and defect spectroscopy, *J. Phys. Chem. Solids*, 2018, **116**, 360–366.

45 Z. Zhou, J. Zheng, R. Shi, N. Zhang, J. Chen, R. Zhang, H. Suo, E. M. Goldys and C. Guo, *Ab initio* site occupancy and far-red emission of Mn^{4+} in cubic-phase $La(MgTi)_{1/2}O_3$ for plant cultivation, *ACS Appl. Mater. Interfaces*, 2017, **9**(7), 6177–6185.

46 A. De, B. Samanta, A. K. Dey, N. Chakraborty, T. K. Parya, S. Saha and U. K. Ghorai, $ZnAl_2O_4$:Eu^{3+} nanoparticle phosphors co-doped with Li^+ for red light-emitting diodes, *ACS Appl. Nano Mater.*, 2021, **5**(1), 331–340.

47 S. Wang, C. Xu and X. Qiao, High thermal stability and color purity of red-emitting phosphor Y_2SiWO_8: Eu^{3+} for w-LEDs: synthesis and photoluminescence properties, *Ceram. Int.*, 2021, **47**(1), 1063–1075.

48 S. Miao, R. Shi, Y. Zhang, D. Chen and Y. Liang, Deep-Red $Ca_3Al_2Ge_3O_{12}$:Eu^{3+} Garnet Phosphor with Near-Unity Internal Quantum Efficiency and High Thermal Stability for Plant Growth Application, *Adv. Mater. Technol.*, 2023, 2202103.

49 J. Huo, A. Yu, Q. Ni, D. Guo, M. Zeng, J. Gao, Y. Zhang and Q. Wang, Efficient energy transfer from trap levels to Eu^{3+} leads to antithermal quenching effect in high-power white light-emitting diodes., *Inorg. Chem.*, 2020, **59**(20), 15514–15525.

50 V. Kumar, S. Som, S. Dutta, S. Das and H. Swart, Red-light-emitting inorganic $La_2Ca_ZnO_5$ frameworks with high photoluminescence quantum efficiency: theoretical approach, *Mater. Des.*, 2016, **93**, 203–215.

51 S. Som, A. Kunti, V. Kumar, V. Kumar, S. Dutta, M. Chowdhury, S. Sharma, J. Terblans and H. Swart, Defect correlated fluorescent quenching and electron phonon coupling in the spectral transition of Eu^{3+} in $CaTiO_3$ for red emission in display application, *J. Appl. Phys.*, 2014, **115**(19), 193101.

52 S. Wang, Y.-j Han, L. Shi, Y.-l Tong, Q.-q Zhao, J.-y Zhang, Z.-y Mao, Z.-f Mu, Z.-w Zhang and S.-l Niu, A new strategy to the phosphors for plant growth LEDs: Far red emission from the $Ca_9MY_{0.667}(PO_4)_7$ (M = Li, Na):Eu^{3+} phosphors due to the Eu^{3+}: $^5D_0 \rightarrow {}^7F_4$ transition, *J. Lumin.*, 2020, **225**, 117404.

53 T. Kurunthatil Kuttiat, M. Abraham, A. K. Kunti, N. Amador-Mendez, M. Tchernycheva and S. Das, Enriching the Deep-Red Emission in $(Mg,Ba)_3M_2GeO_8$: Mn^{4+} (M = Al, Ga) Compositions for Light-Emitting Diodes, *ACS Appl. Mater. Interfaces*, 2023, **15**(5), 7083–7101.